


 Cite this: *RSC Adv.*, 2017, **7**, 54939

## Highly uniform $\text{Fe}_3\text{O}_4$ nanoparticle–rGO composites as anode materials for high performance lithium-ion batteries†

 Shoupu Zhu, Lei Fan  and Yingying Lu \*

Current lithium-ion batteries (LIBs) based on carbonaceous anodes are close to their theoretical performance limits and can hardly meet the demand for high energy applications. Anode materials based on transition metal oxides are promising alternatives to graphite, stemming from their high lithium storage capacity. Among them, iron oxides have the advantages of rich raw materials, low prices, and high theoretical capacities. Herein, we report a facile strategy of improving the capacity and cycling stability of LIBs via the use of reduced graphene oxide-doped  $\text{Fe}_3\text{O}_4$  nanoparticles (around 6.45 nm) as anode materials. Galvanostatic cycling measurements show that cells with  $\text{Fe}_3\text{O}_4$ /rGO nanocomposites deliver a reversible specific capacity of  $1108 \text{ mA h g}^{-1}$  at a current density of  $0.5 \text{ A g}^{-1}$  even after 400 cycles. The unique structure of  $\text{Fe}_3\text{O}_4$ /rGO nanocomposites is responsible for the high cycling performance. The rGO component enables high electrical conductivity while the homogeneous distribution of nano-sized  $\text{Fe}_3\text{O}_4$  in rGO favors the diffusion and charge transfer of ions. The void space amongst the nanoparticles and the rGO nanosheets can accommodate volume expansion during cycling. This novel tactic can be used in the preparation of other transition metal oxides with ultra-small and uniform nanoparticles such as  $\text{SnO}_2$ ,  $\text{Co}_2\text{O}_3$ ,  $\text{TiO}_2$  and  $\text{RuO}_2$  for high-energy LIBs.

Received 25th October 2017  
 Accepted 9th November 2017

DOI: 10.1039/c7ra11779e  
[rsc.li/rsc-advances](http://rsc.li/rsc-advances)

### Introduction

Since the great commercial success of the lithium-ion battery in 1991, there has been dramatic progress in order to satisfy the requirements of fast developing cellphones, electric vehicles, and large-scale energy storage systems. However, conventional lithium-ion batteries that are based on graphite anodes can hardly meet the increasing demand for high-energy, cost-effective, and reliable electrical energy storage. The lithiated graphite anode in currently marketed lithium-ion batteries has a gravimetric capacity of only  $372 \text{ mA h g}^{-1}$ , and lithium-ion battery technology based on carbonaceous materials is approaching its theoretical performance limits. An urgent

requirement for lithium-ion batteries is the exploration of new materials possessing high energy densities that could potentially serve as alternatives for lithium-ion batteries based on this design. New battery technologies such as batteries based on lithium metal or silicon have emerged, targeted on high energy. However, these batteries suffer from intense safety issues, stemming from uneven lithium electrodeposition/formation of lithium dendrites or electrode volume expansion. Lithium-ion batteries are designed for great reliability since lithium ions are hosted in a supporting material, preventing formation of lithium dendrites and reducing the huge volume expansion.

Transition metal oxides as anodes for lithium-ion batteries have received much attention since 2000 when Poizot *et al.* first reported their high lithium storage capacity and special conversion mechanism.<sup>1</sup> The challenges for transition metal oxides are often associated with the large voltage hysteresis, which limits the energy efficiency of electrochemical redox reactions.<sup>2–5</sup> Although the mechanism is still not clear, it could be due to the poor electronic conductivity, the slow charge transfer kinetics and the structural instability.<sup>6–11</sup> Most of the cells using transition metal oxides display voltage hysteresis from 0.7 to 1.0 V, among which cells with iron oxide/rGO show a lower overpotential of around 0.7 V. Studies show that three-dimensional electrode materials can effectively reduce the voltage hysteresis. Wang *et al.* fabricated cells with 3D meso-structured Ni scaffolded  $\text{Fe}_2\text{O}_3$  electrodes, whose voltage hysteresis is 0.62 V at  $100 \text{ mA g}^{-1}$  and can be further reduced to

State Key Laboratory of Chemical Engineering, Institute of Pharmaceutical Engineering, College of Chemical and Biological Engineering, Zhejiang University, Hangzhou 310027, China. E-mail: [yingyinglu@zju.edu.cn](mailto:yingyinglu@zju.edu.cn); Tel: +86-0571-87953906

† Electronic supplementary information (ESI) available: TEM and SEM images, and XRD patterns of  $\text{Fe}(\text{OH})_3$ /GO with or without adding hydrazine (Fig. S1); TEM images of  $\text{Fe}_3\text{O}_4$ /rGO-180 and  $\text{Fe}_2\text{O}_3$ /rGO, and the XRD pattern of  $\text{Fe}_2\text{O}_3$ /rGO (Fig. S2); BET surface areas of  $\text{Fe}_3\text{O}_4$ , rGO and  $\text{Fe}_3\text{O}_4$ /rGO (Fig. S3); TEM images of  $\text{Fe}_3\text{O}_4$  nanoparticles at different magnifications (Fig. S4); a TEM image of  $\text{Fe}_3\text{O}_4$ /rGO-180 and SEM images of  $\text{Fe}_3\text{O}_4$ /rGO at different magnifications (Fig. S5); the first cycle charge–discharge profiles of cells with  $\text{Fe}_3\text{O}_4$ , rGO,  $\text{Fe}_3\text{O}_4$ /rGO-180 or  $\text{Fe}_3\text{O}_4$ /rGO (Fig. S6); coulombic efficiencies of cells with rGO,  $\text{Fe}_3\text{O}_4$ ,  $\text{Fe}_3\text{O}_4$ /rGO-180 or  $\text{Fe}_3\text{O}_4$ /rGO at a current density of  $0.5 \text{ A g}^{-1}$  and long-term charge–discharge coulombic efficiencies of cells with  $\text{Fe}_3\text{O}_4$  or  $\text{Fe}_3\text{O}_4$ /rGO (Fig. S7); the equivalent circuit used for fitting cell resistances (Fig. S8). See DOI: [10.1039/c7ra11779e](https://doi.org/10.1039/c7ra11779e)



0.42 V at elevated temperature.<sup>3</sup> In addition, iron oxides have the advantages of rich raw materials, low prices, and high theoretical capacities (1007 mA h g<sup>-1</sup> for  $\alpha$ -Fe<sub>2</sub>O<sub>3</sub> and 926 mA h g<sup>-1</sup> for Fe<sub>3</sub>O<sub>4</sub>). However, common iron oxides often undergo large volume changes (193% for Fe<sub>2</sub>O<sub>3</sub>, calculated from the densities of Fe<sub>2</sub>O<sub>3</sub>, Fe and Li<sub>2</sub>O) based on their electrochemical reactions in the charging–discharging process,<sup>12,13</sup> which can cause crushing of the crystal and aggregation of particles and lead to almost constantly falling capacity decay during the initial few cycles. Fortunately, the electrochemical performance can be effectively improved by combining iron oxides with conducting materials<sup>14</sup> such as reduced graphene oxide (rGO),<sup>15–18</sup> carbon,<sup>19–22</sup> carbon nanofibers (CNFs),<sup>23,24</sup> carbon nanotubes,<sup>25,26</sup> and conductive polymers.<sup>27,28</sup> Coating carbon materials or conductive polymers can fix the locations of iron oxides in the composite electrode, buffer the volume expansion and shrinkage, and retain the integrity of the crystal structures. The highly conductive nature of the coating materials can also remedy the weak conductivity of iron oxides and improve the transport properties of lithium ions. On the other hand, the morphology of iron oxides is also critical to the electrochemical performance, and structural modifications on iron oxides such as three-dimensional  $\alpha$ -Fe<sub>2</sub>O<sub>3</sub>,<sup>29</sup> porous  $\alpha$ -Fe<sub>2</sub>O<sub>3</sub><sup>30</sup> and  $\alpha$ -Fe<sub>2</sub>O<sub>3</sub> nanoflakes<sup>31</sup> have been proven to stabilize the cycling behavior and increase the lithium storage capacity. Iron oxides with small particle size possess large specific surface areas, facilitating the contact between electrode and electrolyte, and shortening the diffusion path of lithium ions in the vicinity of the electrode. The void space amongst the nano-sized particles can accommodate the volume expansion and maintain the structural stability during cycling. The uniform particle size can generate uniform stress/strain over the entire electrode, preventing local cracking of the electrode during the lithiation and delithiation processes.<sup>32</sup>

Owing to its excellent electrochemical properties such as high electrical conductivity and high lithium storage capacity,<sup>15</sup> graphene has attracted great research interest for application in lithium-ion batteries. For the fabrication of graphene, oxygen-containing groups such as C–O–C, –OH and –COOH are often introduced onto the surface of graphene to yield graphene oxide (GO). This enables good solubility in water, generates an electrostatic force with the electropositive groups and forms assembled nanocomposites. Therefore, Fe<sub>x</sub>O<sub>y</sub>/rGO composites using GO as a precursor for rGO have been fabricated for lithium-ion batteries.<sup>17,18,33–36</sup> However, the precursors used for the preparation, which are important for exploring the reaction mechanisms, have rarely been discussed in previous literature. Additionally, Fe<sub>x</sub>O<sub>y</sub>/rGO with nano-sized (typically less than 10 nm) iron oxides that uniformly anchor on the surface of the rGO nanosheet has rarely been reported. Herein, we report a facile strategy of improving the capacity and cycling stability of lithium-ion batteries *via* the use of rGO doped Fe<sub>3</sub>O<sub>4</sub> nanoparticles as anode materials. Different precursors for making the iron oxides were extensively discussed and ultra-small iron oxides were successfully prepared, uniformly embedded in rGO nanosheets.

## Experimental section

### Synthesis of Fe<sub>3</sub>O<sub>4</sub>, rGO, Fe<sub>3</sub>O<sub>4</sub>/rGO-180, Fe<sub>3</sub>O<sub>4</sub>/rGO, Fe<sub>2</sub>O<sub>3</sub>/rGO and Fe(OH)<sub>3</sub>/GO

0.5 mL FeCl<sub>3</sub> solution (2 mol L<sup>-1</sup>) was added to 20 mL boiling deionized (DI) water drop by drop, and the solution was kept boiling for about 3 minutes to yield the Fe(OH)<sub>3</sub> sol. 80 mg graphene oxide was mixed with 20 mL DI water and the solution was then ultrasonically dispersed for 120 min to ensure the uniform distribution of graphene oxide nanosheets in DI water. The Fe(OH)<sub>3</sub> sol and graphene oxide solution were mixed together by vigorous stirring. Then 1 mmol vitamin C and 1.25 mL hydrogen were successively added into the mixture. After stirring for 15 minutes, the mixed solution was transferred into a 50 mL Teflon-lined stainless steel autoclave and heated at 180 °C for 12 h in a drying oven. The precipitate was collected and washed with DI water until the supernatant liquid was clear. Then the Fe<sub>3</sub>O<sub>4</sub>/rGO-180 was obtained after freeze drying. The Fe<sub>2</sub>O<sub>3</sub>/rGO was prepared *via* the same process without adding vitamin C, and pure Fe<sub>3</sub>O<sub>4</sub> and rGO were fabricated in the absence of GO and Fe(OH)<sub>3</sub>, respectively. Fe<sub>3</sub>O<sub>4</sub>/rGO-180 was further calcined at 500 °C for 2 h in an Ar atmosphere with a heating rate of 5 °C min<sup>-1</sup>, to yield Fe<sub>3</sub>O<sub>4</sub>/rGO. Fe(OH)<sub>3</sub>/GO nanocomposites were collected from centrifuging the mixed solution of the Fe(OH)<sub>3</sub> sol and the GO solution.

### Materials characterization

TGA was performed in an air atmosphere from room temperature to 800 °C at a heating rate of 10 °C min<sup>-1</sup> on a PE TGA7 thermal analyzer. Powder XRD measurements were carried out in a PANalytical X'Pert PRO X-ray diffractometer with Cu-K $\alpha$  radiation at a scanning rate of 10° min<sup>-1</sup>. XPS measurements were carried out in a VG ESCALAB spectrometer with an Al-K $\alpha$  (1486.8 eV) X-ray source to characterize the crystal phase of the iron oxide. SEM was performed with a Hitachi SU8010 scanning electron micro-analyzer with an accelerating voltage of 5 kV. TEM was conducted at 200 kV with a Philips TECNAI 12 field emission microscope. Raman spectra were recorded by a Horiba Jobin Yvon LabRAM HR Evolution Raman spectrometer with 532 nm wavelength. The Brunauer–Emmett–Teller (BET) surface areas of the samples were measured using a Micromeritics TriStar II porosity and surface area analyzer. The resistances of Fe<sub>3</sub>O<sub>4</sub>, Fe<sub>3</sub>O<sub>4</sub>/rGO-180 and Fe<sub>3</sub>O<sub>4</sub>/rGO were tested using a 4 Probes Tech ST-21 four-point probe square resistance tester.

### Electrochemical measurements

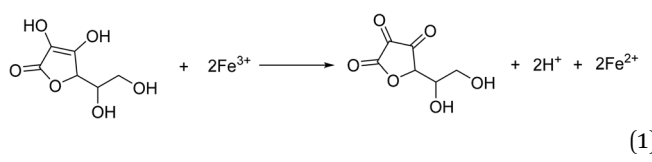
CR 2032 coin cells were used to measure the electrochemical performance of Fe<sub>3</sub>O<sub>4</sub>, rGO, Fe<sub>3</sub>O<sub>4</sub>/rGO-180 and Fe<sub>3</sub>O<sub>4</sub>/rGO. The working electrode consists of 80 wt% of active material (about 1–2 mg), 10 wt% of super P conductive carbon black and 10 wt% of PVDF. Cu foil was used as the current collector. The assembly was carried out in a high-purity argon-filled glovebox, using a lithium plate as the counter/reference electrode, Celgard 2400 polypropylene as the separator, and 1 M LiPF<sub>6</sub> in a mixture of ethylene carbonate (EC), diethyl carbonate (DMC) and ethyl-



methyl carbonate (EMC) (1 : 1 : 1 by volume) as the electrolyte. Galvanostatic charge and discharge cycling of the cells was performed using a Land CT2001A battery test system. Cyclic voltammetry (CV) measurements and electrochemical impedance spectroscopic (EIS) measurements were conducted on a Solartron Analytical 1400 CellTest System.

## Results and discussion

The synthesis procedure is schematically depicted in Fig. 1. As the surface of the GO nanosheets has oxygen-containing groups,  $\text{Fe(OH)}_3$  nanoparticles can be uniformly adsorbed on the surface, forming  $\text{Fe(OH)}_3/\text{GO}$  nanocomposites under electrostatic force,<sup>37</sup> which was verified by transmission electron microscopy (TEM) and scanning electron microscopy (SEM) analyses (Fig. S1a–c†). The homogeneously attached  $\text{Fe(OH)}_3$  nanoparticles were created for uniform  $\text{Fe}_3\text{O}_4$  loading during the subsequent reactions. Additionally, hydrazine was added for the pre-reduction of  $\text{Fe(OH)}_3/\text{GO}$ , and the GO in  $\text{Fe(OH)}_3/\text{GO}$  was slightly reduced, which is demonstrated by the X-ray diffraction (XRD) patterns in Fig. S1d.† The XRD pattern for the  $\text{Fe(OH)}_3/\text{GO}$  mixture shows a strong characteristic diffraction peak at about  $11.0^\circ$ , which disappeared after the addition of hydrazine. It indicates that hydrazine can partially reduce GO by simply stirring the mixed solution at room temperature. After vitamin C and hydrazine were added to the solution, the  $\text{Fe(OH)}_3$  nanoparticles were transformed into  $\text{Fe}_3\text{O}_4$  nanoparticles and the partially reduced GO was fully transformed to rGO *via* the hydrothermal reaction. The product is named as  $\text{Fe}_3\text{O}_4/\text{rGO-180}$ . During the process,  $\text{Fe}^{3+}$  can be reduced to  $\text{Fe}^{2+}$  by the reductant VC ( $\text{H}_2\text{A}$ ) *via* reaction (1)<sup>38</sup> and GO is understood to be reduced by hydrazine to rGO.<sup>33,34</sup>



We also compared  $\text{Fe}_2\text{O}_3/\text{rGO}$  produced from a hydrothermal reaction with  $\text{Fe(OH)}_3$  and GO as precursors and hydrazine as a reductant (Fig. S2a and b†). This shows that

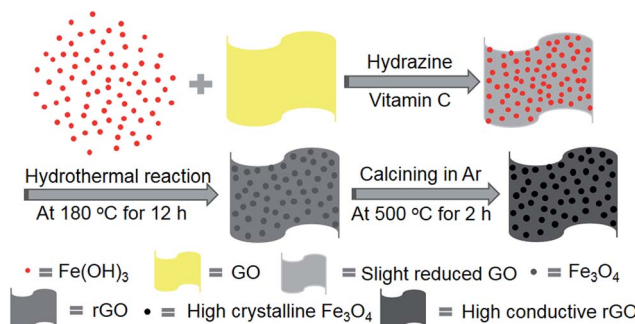


Fig. 1 Schematic illustration of the preparation of the two-dimensional  $\text{Fe}_3\text{O}_4/\text{rGO}$  composite electrode.

employing VC as the reducing agent not only yields  $\text{Fe}_3\text{O}_4$  but also enables the formation of iron oxides with smaller particle sizes. The reductive product formed using bare hydrazine is  $\text{Fe}_2\text{O}_3$ , which was verified by XRD analysis (Fig. S2c†). To further enhance the electrical conductivity of rGO and increase the crystallinity of  $\text{Fe}_3\text{O}_4$ , the  $\text{Fe}_3\text{O}_4/\text{rGO-180}$  was calcined at  $500^\circ\text{C}$  under argon gas protection. The as-prepared  $\text{Fe}_3\text{O}_4/\text{rGO}$  shows a uniform morphology consisting of  $\text{Fe}_3\text{O}_4$  with increased crystallinity and rGO with enhanced conductivity. Brunauer–Emmett–Teller (BET) measurement was conducted to measure the surface areas of  $\text{Fe}_3\text{O}_4$ , rGO and  $\text{Fe}_3\text{O}_4/\text{rGO}$  (Fig. S3†). It showed that  $\text{Fe}_3\text{O}_4/\text{rGO}$  has a BET surface area of  $114.7\text{ m}^2\text{ g}^{-1}$  which is higher than that for  $\text{Fe}_3\text{O}_4$  and rGO. The void space amongst the nano-sized  $\text{Fe}_3\text{O}_4$  particles allows the diffusion and migration of ions and can also buffer the volume changes during cycling.

Further evidence of the successful synthesis of the  $\text{Fe}_3\text{O}_4/\text{rGO}$  composites is provided by XRD and X-ray photoelectron spectroscopy (XPS) analyses. Fig. 2a shows the XRD patterns of rGO,  $\text{Fe}_3\text{O}_4$ ,  $\text{Fe}_3\text{O}_4/\text{rGO}$  and  $\text{Fe}_3\text{O}_4/\text{rGO-180}$ . The identified diffraction peaks of  $\text{Fe}_3\text{O}_4$  are indexed to the standard card of magnetic  $\text{Fe}_3\text{O}_4$  (JCPDS card no. 19-0629) and no additional peak is detected, implying the high purity of  $\text{Fe}_3\text{O}_4$ . The identifying peaks of rGO at about  $26.4^\circ$  and  $44.4^\circ$  are assigned to the (002) and (101) lattice planes of hexagonal graphite (JCPDS card no. 41-1487), respectively. Other than the peaks for  $\text{Fe}_3\text{O}_4$ ,  $\text{Fe}_3\text{O}_4/\text{rGO-180}$  has an extra peak at about  $26.4^\circ$  corresponding to the above-mentioned (002) lattice plane in graphite. This indicates that  $\text{Fe}_3\text{O}_4/\text{rGO-180}$  contains both  $\text{Fe}_3\text{O}_4$  and rGO. All of the diffraction peaks which emerge for  $\text{Fe}_3\text{O}_4/\text{rGO-180}$  become stronger in the XRD pattern of  $\text{Fe}_3\text{O}_4/\text{rGO}$ , showing that the calcination of  $\text{Fe}_3\text{O}_4/\text{rGO-180}$  increases the crystallinity of  $\text{Fe}_3\text{O}_4$  and enhances the degree of reduction of rGO. The chemical composition of the as-prepared  $\text{Fe}_3\text{O}_4/\text{rGO-180}$  was further determined by XPS analysis. The peak binding energies of 711.5 and 724.9 eV in Fig. 2b are associated with  $\text{Fe} 2p_{3/2}$  and  $\text{Fe} 2p_{1/2}$  in  $\text{Fe}_3\text{O}_4/\text{rGO-180}$ , respectively. This demonstrates the existence of  $\text{Fe}_3\text{O}_4$  in  $\text{Fe}_3\text{O}_4/\text{rGO-180}$ , consistent with previous reports.<sup>15,19,39</sup>

The weight fractions of  $\text{Fe}_3\text{O}_4$  and rGO in  $\text{Fe}_3\text{O}_4/\text{rGO-180}$  and  $\text{Fe}_3\text{O}_4/\text{rGO}$  were characterized by thermogravimetric (TG) analysis in air. During the thermal process, the amount of  $\text{Fe}_2\text{O}_3$  should be 1.035 times the amount of  $\text{Fe}_3\text{O}_4$ , calculated from the reaction of  $4\text{Fe}_3\text{O}_4 + \text{O}_2 = 6\text{Fe}_2\text{O}_3$ , and rGO would convert to  $\text{CO}_2$ . Therefore, according to the ratio of the residual reddish brown  $\text{Fe}_2\text{O}_3$  in the original  $\text{Fe}_3\text{O}_4/\text{rGO-180}$  shown in Fig. 2c, the calculated proportions of  $\text{Fe}_3\text{O}_4$  and rGO in  $\text{Fe}_3\text{O}_4/\text{rGO-180}$  are 43.9 wt% and 56.1 wt%, respectively. Additionally, the proportions of  $\text{Fe}_3\text{O}_4$  and rGO in  $\text{Fe}_3\text{O}_4/\text{rGO}$  were calculated to be 57.7 wt% and 42.3 wt%, respectively. The results indicate that the  $\text{Fe}_3\text{O}_4/\text{rGO}$  contains more  $\text{Fe}_3\text{O}_4$  and thus more rGO with a higher level of reduction. Fig. 2d shows the Raman spectra of GO, rGO,  $\text{Fe}_3\text{O}_4/\text{rGO-180}$  and  $\text{Fe}_3\text{O}_4/\text{rGO}$ . This allows us to assess the degree of disorder in the carbon materials. The spectra of these four materials show two pronounced peaks: a D peak at about  $1350\text{ cm}^{-1}$  and a G peak at about  $1590\text{ cm}^{-1}$ . The D peak corresponds to the disordered structures with defects,



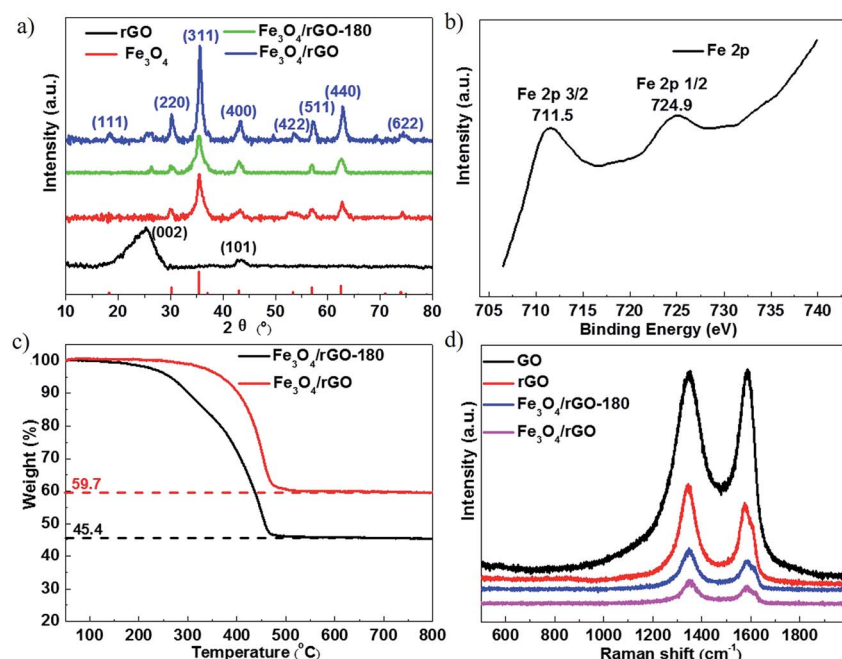


Fig. 2 (a) XRD patterns of rGO, Fe<sub>3</sub>O<sub>4</sub>, Fe<sub>3</sub>O<sub>4</sub>/rGO-180 and Fe<sub>3</sub>O<sub>4</sub>/rGO. (b) The high resolution Fe 2p spectrum of Fe<sub>3</sub>O<sub>4</sub>/rGO-180. (c) TG curves of Fe<sub>3</sub>O<sub>4</sub>/rGO-180 and Fe<sub>3</sub>O<sub>4</sub>/rGO. (d) Raman spectra of GO, rGO, Fe<sub>3</sub>O<sub>4</sub>/rGO-180 and Fe<sub>3</sub>O<sub>4</sub>/rGO.

while the graphitic structures with order are responsible for the G peak. The degree of disorder in the carbon materials is often determined from the ratio of the peak intensities ( $R$ ),  $I_D/I_G$ . The values of  $R$  for GO and rGO are 1.00 and 1.26, respectively. It should be noted that Fe<sub>3</sub>O<sub>4</sub> has a peak at about 1300 cm<sup>-1</sup>, thus the values of  $R$  for Fe<sub>3</sub>O<sub>4</sub>/rGO-180 and Fe<sub>3</sub>O<sub>4</sub>/rGO are difficult to calculate.<sup>33</sup> The increased value of  $R$  in rGO reflects the presence of more disorder or carbon defects.<sup>40-42</sup>

Fig. 3a and c show the morphologies of Fe<sub>3</sub>O<sub>4</sub>/rGO-180 and Fe<sub>3</sub>O<sub>4</sub>/rGO. They demonstrate that Fe<sub>3</sub>O<sub>4</sub> nanoparticles are uniformly embedded in rGO nanosheets. The morphology of the composite electrode created using Fe(OH)<sub>3</sub> is more uniform than that using FeCl<sub>3</sub>·6H<sub>2</sub>O as a precursor.<sup>43</sup> We also created pure Fe<sub>3</sub>O<sub>4</sub> nanoparticles using hydrazine and VC at 180 °C and they display similar morphology to the nanoparticles in Fe<sub>3</sub>O<sub>4</sub>/rGO-180 (Fig. S4a and b†). Fig. 3b and d show the particle diameter distribution of Fe<sub>3</sub>O<sub>4</sub> nanoparticles in Fe<sub>3</sub>O<sub>4</sub>/rGO-180 and Fe<sub>3</sub>O<sub>4</sub>/rGO. These show that the average size of Fe<sub>3</sub>O<sub>4</sub> in Fe<sub>3</sub>O<sub>4</sub>/rGO-180 is 6.42 nm with a diameter range from 4.1 to 8.8 nm, and the average size of Fe<sub>3</sub>O<sub>4</sub> in Fe<sub>3</sub>O<sub>4</sub>/rGO is 6.45 nm with a diameter range from 3.9 to 9.6 nm. The low magnification TEM image of Fe<sub>3</sub>O<sub>4</sub>/rGO-180 and the SEM images of Fe<sub>3</sub>O<sub>4</sub>/rGO further confirm the uniform distribution of Fe<sub>3</sub>O<sub>4</sub> in rGO (Fig. S5a–c†).

Fig. 4 shows the electrochemical cycling performance of cells with rGO, Fe<sub>3</sub>O<sub>4</sub>, Fe<sub>3</sub>O<sub>4</sub>/rGO-180 and Fe<sub>3</sub>O<sub>4</sub>/rGO as the electrode. Fig. 4a compares the cycling performance of the first 100 cycles of the four electrodes. The cells with Fe<sub>3</sub>O<sub>4</sub>/rGO-180 or Fe<sub>3</sub>O<sub>4</sub>/rGO have much higher charge–discharge capacities than the cells with rGO or Fe<sub>3</sub>O<sub>4</sub>, indicating that the employment of rGO with Fe<sub>3</sub>O<sub>4</sub> nanoparticles increases the capacity compared

to bare Fe<sub>3</sub>O<sub>4</sub>. It can also be seen that the cells with Fe<sub>3</sub>O<sub>4</sub>/rGO display a higher capacity than the cells with Fe<sub>3</sub>O<sub>4</sub>/rGO-180, meaning that the calcination process used to make Fe<sub>3</sub>O<sub>4</sub>/rGO is responsible for the enhancement in cycling performance. This might be due to the increased crystallinity of Fe<sub>3</sub>O<sub>4</sub> and the increased degree of graphitization of rGO. Fig. 4a also shows that the capacities of the cells with Fe<sub>3</sub>O<sub>4</sub>/rGO-180 or Fe<sub>3</sub>O<sub>4</sub>/rGO decrease dramatically in the first 10 cycles and gradually increase during the subsequent cycles. It should be noted that the capacity after the initial decrease can be higher than the theoretical specific capacity of Fe<sub>3</sub>O<sub>4</sub>/rGO (around 849.6 mA h g<sup>-1</sup>). The exceeded capacity is attributed to the reversible formation of a polymeric gel-like film,<sup>44–47</sup> which grows continuously and delivers additional reversible capacity after the first few cycles. The charge–discharge voltage profiles for the four electrodes at the first cycle are provided in Fig. S6.† The long-term charge–discharge characteristics of cells with Fe<sub>3</sub>O<sub>4</sub> or Fe<sub>3</sub>O<sub>4</sub>/rGO are shown in Fig. 4b. The discharge capacities of Fe<sub>3</sub>O<sub>4</sub>/rGO at the 100<sup>th</sup>, 150<sup>th</sup>, 250<sup>th</sup> and 400<sup>th</sup> cycles are 1126, 1143, 1193 and 1108 mA h g<sup>-1</sup>, respectively, while those of Fe<sub>3</sub>O<sub>4</sub> at the 150<sup>th</sup>, 200<sup>th</sup>, 250<sup>th</sup> and 300<sup>th</sup> cycles are 128, 149, 173 and 192 mA h g<sup>-1</sup>, respectively. This indicates that Fe<sub>3</sub>O<sub>4</sub>/rGO delivers higher capacity than bare Fe<sub>3</sub>O<sub>4</sub>, and has good capacity retention for deep cycling. The coulombic efficiencies of these four electrodes are displayed in Fig. S7.† The rate capability of cells with Fe<sub>3</sub>O<sub>4</sub>/rGO is measured by galvanostatically cycling the cells at different current densities, as shown in Fig. 4c. Cells with Fe<sub>3</sub>O<sub>4</sub>/rGO render high specific discharge capacities of 1188, 1086, 1011, 903, 811, 718 and 593 mA h g<sup>-1</sup> at current densities of 0.05, 0.1, 0.2, 0.5, 1.0, 2.0 and 5.0 A g<sup>-1</sup>, respectively. Additionally, when cycled back to

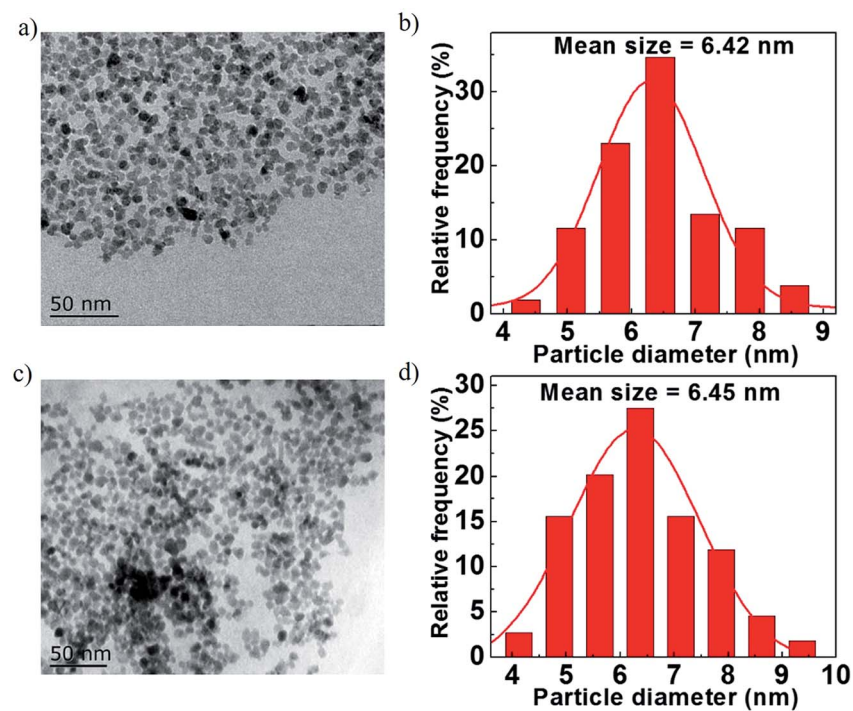


Fig. 3 (a and c) TEM images of  $\text{Fe}_3\text{O}_4/\text{rGO-180}$  and  $\text{Fe}_3\text{O}_4/\text{rGO}$ . (b and d) The diameter distribution of  $\text{Fe}_3\text{O}_4$  nanoparticles in  $\text{Fe}_3\text{O}_4/\text{rGO-180}$  and  $\text{Fe}_3\text{O}_4/\text{rGO}$ .

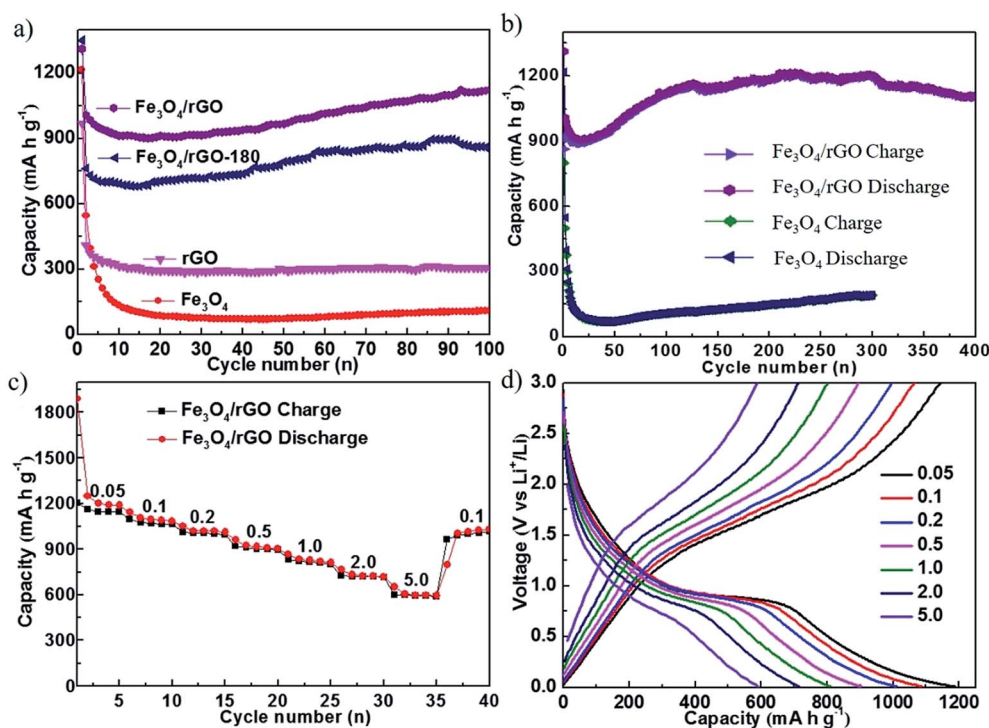


Fig. 4 (a) The cycling performance of cells with rGO,  $\text{Fe}_3\text{O}_4$ ,  $\text{Fe}_3\text{O}_4/\text{rGO-180}$  and  $\text{Fe}_3\text{O}_4/\text{rGO}$  at a current density of  $0.5 \text{ A g}^{-1}$ . (b) The long-term charge-discharge characteristics of cells using  $\text{Fe}_3\text{O}_4$  and  $\text{Fe}_3\text{O}_4/\text{rGO}$ . (c) The rate capability of cells with the  $\text{Fe}_3\text{O}_4/\text{rGO}$  electrode. The galvanostatic cycling measurements were performed at various current densities from  $0.05 \text{ A g}^{-1}$  to  $5 \text{ A g}^{-1}$ . (d) The corresponding charge-discharge curves of (c).

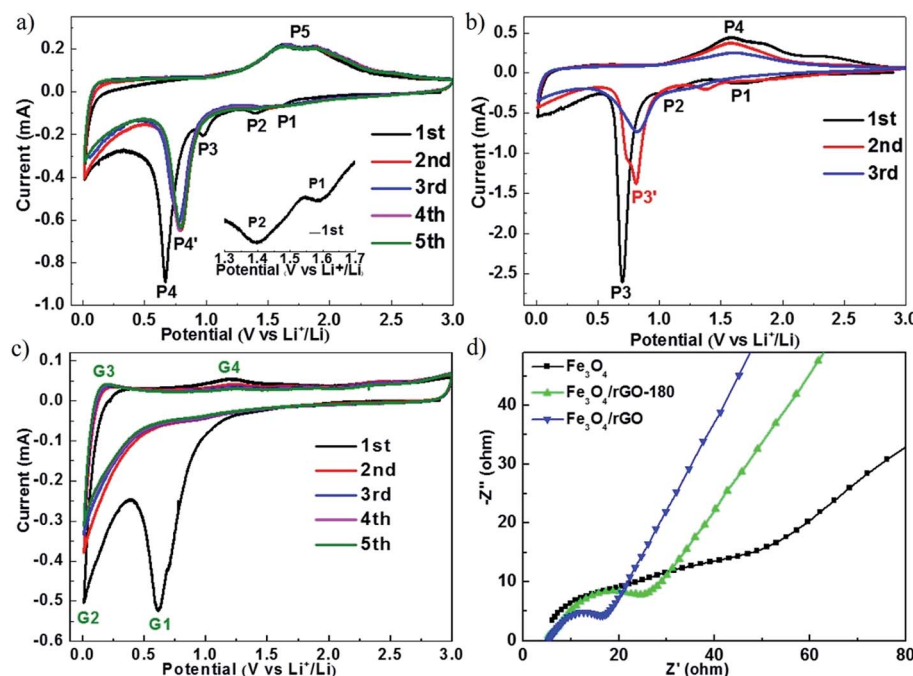


Fig. 5 CV curves of (a)  $\text{Fe}_3\text{O}_4/\text{rGO}$ , (b)  $\text{Fe}_3\text{O}_4$  and (c) rGO at a scan rate of  $0.1 \text{ mV s}^{-1}$  in a voltage range of  $0.01$ – $3.0 \text{ V}$ . (d) Nyquist plots of  $\text{Fe}_3\text{O}_4$ ,  $\text{Fe}_3\text{O}_4/\text{rGO-180}$  and  $\text{Fe}_3\text{O}_4/\text{rGO}$ .

a lower current density of  $0.1 \text{ A g}^{-1}$ , the cell maintains the initial discharge capacity and delivers  $1030 \text{ mA h g}^{-1}$ . Fig. 4d shows the corresponding specific charge–discharge curves of cells using  $\text{Fe}_3\text{O}_4/\text{rGO}$  at different current densities. The approximate symmetrical shapes of these curves indicate good reversibility of  $\text{Li}^+$  insertion/extraction.

Fig. 5a–c show the cyclic voltammograms (CVs) of cells with  $\text{Fe}_3\text{O}_4/\text{rGO}$ ,  $\text{Fe}_3\text{O}_4$  and rGO, respectively. The electrochemical measurements were carried out at a voltage of  $0.01$ – $3.00 \text{ V}$  and at a scan rate of  $0.1 \text{ mV s}^{-1}$ . During the first cycle, the cathodic peaks were observed at about  $1.59 \text{ V}$  (P1),  $1.37 \text{ V}$  (P2) and  $1.00 \text{ V}$  (P3), which are assigned to the reaction  $\text{Fe}_3\text{O}_4 + x\text{Li}^+ + xe^- \rightarrow \text{Li}_x\text{Fe}_3\text{O}_4$ ,<sup>20–22</sup> and the peak at about  $0.67 \text{ V}$  (P4) is attributed to the reaction  $\text{Li}_x\text{Fe}_3\text{O}_4 + (8 - x)\text{Li}^+ + (8 - x)e^- \rightarrow 3\text{Fe}^0 + 4\text{Li}_2\text{O}$  and the generation of a solid electrolyte interface (SEI) film.<sup>20–22</sup> The broad anodic peak (P5) containing two connected peaks at about  $1.63 \text{ V}$  and  $1.87 \text{ V}$  is attributed to the oxidation reactions of  $\text{Fe}^0$  to  $\text{Fe}^{2+}$  and  $\text{Fe}^{2+}$  to  $\text{Fe}^{3+}$ , respectively.<sup>26,47</sup> During the subsequent cycles, the cathodic peak P4 shifts to  $0.79 \text{ V}$ , which is due to the diminished polarization effect.<sup>37</sup> It can also be seen that there are no visibly pronounced changes in the peak position and current amplitude after the first cycle, indicating that  $\text{Fe}_3\text{O}_4/\text{rGO}$  has excellent cycling stability. Fig. 5b summarizes the CVs of cells with  $\text{Fe}_3\text{O}_4$  for the first three cycles. The peak corresponding to the reaction of  $\text{Fe}_3\text{O}_4$  to  $\text{Fe}$  is at about  $0.70 \text{ V}$  (P3) and the peaks for the reverse reaction appear at about  $1.62 \text{ V}$  and  $1.82 \text{ V}$  (P4) in the first cycle. These peak currents continuously decline in the 2<sup>nd</sup> and 3<sup>rd</sup> cycles, which could be caused by crushing of the crystal, volume expansion and shrinkage of  $\text{Fe}_3\text{O}_4$  and the continuous breaking and formation of the SEI film.<sup>14</sup> Fig. 5c shows the CVs for cells with

rGO. The peak at about  $0.19 \text{ V}$  corresponds to the extraction of lithium ions from graphitized carbon, and the anodic peak at about  $1.22 \text{ V}$  corresponds to the irreversible reaction with the electrolyte.<sup>24</sup>

The electrochemical resistances for cells with  $\text{Fe}_3\text{O}_4$ ,  $\text{Fe}_3\text{O}_4/\text{rGO-180}$  and  $\text{Fe}_3\text{O}_4/\text{rGO}$  were monitored after one charge–discharge cycle at  $0.5 \text{ A g}^{-1}$ , as shown in Fig. 5d. The measurements were conducted at an open circuit potential with an AC voltage amplitude of  $5.0 \text{ mV}$  from  $100 \text{ kHz}$  to  $0.01 \text{ Hz}$ . The start of the semicircle is associated with the electrolyte resistance ( $R_s$ ), the semicircle at high frequency corresponds to the charge transfer resistance ( $R_{ct}$ ) and the line near the end of the semicircle reveals the diffusion of lithium ions. The electrolyte resistances are almost the same for the three types of cell, and cells with  $\text{Fe}_3\text{O}_4/\text{rGO-180}$  or  $\text{Fe}_3\text{O}_4/\text{rGO}$  have a much smaller  $R_{ct}$  than cells with  $\text{Fe}_3\text{O}_4$ . This indicates that the combination of  $\text{Fe}_3\text{O}_4$  with rGO promotes the charge transfer kinetics and the diffusion of lithium ions in the vicinity of the electrode. The equivalent circuit is used for fitting (Fig. S8†).

## Conclusions

In summary, we fabricated a uniform  $\text{Fe}_3\text{O}_4/\text{reduced graphene oxide}$  nanocomposite electrode by a hydrothermal reaction using  $\text{Fe}(\text{OH})_3$  and graphene oxide as precursors, and vitamin C and hydrazine as reductants. The oxygen containing groups in the graphene oxide nanosheets facilitated the uniform distributions of  $\text{Fe}(\text{OH})_3$  nanoparticles on the surfaces of rGO via electrostatic forces.  $\text{Fe}_3\text{O}_4/\text{rGO}$  nanoparticles were further calcined to increase the crystallinity of  $\text{Fe}_3\text{O}_4$  and to increase the degree of graphitization of rGO. From electrochemical



measurements, it was found that cells using  $\text{Fe}_3\text{O}_4$ /rGO nanoparticles as the electrode deliver a reversible capacity of 1108  $\text{mA h g}^{-1}$  after 400 cycles at 0.5  $\text{A g}^{-1}$  and maintain a reversible capacity of 593  $\text{mA h g}^{-1}$  at a high current density of 5.0  $\text{A g}^{-1}$ . The tiny particle size and uniform particle distribution of  $\text{Fe}_3\text{O}_4$  in rGO are responsible for the excellent electrochemical performance. The void space amongst the  $\text{Fe}_3\text{O}_4$  nanoparticles and rGO serves as a reservoir for the volume changes during cycling, and the graphitized nature of rGO remedies the weak conductivity of iron oxides. This novel synthesis method can potentially be applied to other transition metal oxides such as  $\text{SnO}_2$ ,  $\text{Co}_2\text{O}_3$ ,  $\text{NiO}$ ,  $\text{TiO}_2$  and  $\text{RuO}_2$  for high-energy lithium-ion batteries.

## Conflicts of interest

The authors declare no competing financial interest.

## Acknowledgements

Y. Lu acknowledges the financial support from the National Key R&D Program of China (2016YFA0202900), the Natural Science Foundation of China (NSFC, grant number 21676242), and the State Key Laboratory of Chemical Engineering (No. SKL-ChE-17D01). Y. Lu appreciates the help from Yongjuan Xie and Jingjing Hua for the TEM and SEM characterization in the Test Center of Yangzhou University.

## References

- 1 P. Poizot, S. Laruelle, S. Grugeon, L. Dupont and J. M. Tarascon, *Nature*, 2000, **407**, 496–499.
- 2 L. Taberna, S. Mitra, P. Poizot, P. Simon and J. M. Tarascon, *Nat. Mater.*, 2006, **5**, 567–573.
- 3 J. J. Wang, H. Zhou, J. Nanda and P. V. Braun, *Chem. Mater.*, 2015, **27**, 2803–2811.
- 4 M. V. Reddy, C. Yu, J. H. Fan, K. P. Loh and B. V. R. Chowdari, *ACS Appl. Mater. Interfaces*, 2013, **5**, 4361–4366.
- 5 Y. Sharma, N. Sharma, G. V. S. Rao and B. V. R. Chowdari, *J. Power Sources*, 2007, **173**, 495–501.
- 6 S. K. Martha, J. Nanda, H. Zhou, J. C. Idrobo, N. J. Dudney, S. Pannala, S. Dai, J. J. Wang and P. V. Braun, *RSC Adv.*, 2014, **4**, 6730–6737.
- 7 X. P. Gao and H. X. Yang, *Energy Environ. Sci.*, 2010, **3**, 174–189.
- 8 J. Cabana, L. Monconduit, D. Larcher and M. R. Palacin, *Adv. Mater.*, 2010, **22**, E170–E192.
- 9 R. E. Doe, K. A. Persson, Y. S. Meng and G. Ceder, *Chem. Mater.*, 2008, **20**, 5274–5283.
- 10 N. Yamakawa, M. Jiang, B. Key and C. P. Grey, *J. Am. Chem. Soc.*, 2009, **131**, 10525–10536.
- 11 F. Wang, H. C. Yu, M. H. Chen, L. J. Wu, N. Pereira, K. Thornton, A. Van der Ven, Y. M. Zhu, G. G. Amatucci and J. Graetz, *Nat. Commun.*, 2012, **3**, 8.
- 12 J. Jiang, Y. Y. Li, J. P. Liu, X. T. Huang, C. Z. Yuan and X. W. Lou, *Adv. Mater.*, 2012, **24**, 5166–5180.
- 13 H. W. Zhang, L. Zhou, O. Noonan, D. J. Martin, A. K. Whittaker and C. Z. Yu, *Adv. Funct. Mater.*, 2014, **24**, 4337–4342.
- 14 H. B. Wu, J. S. Chen, H. H. Hng and X. W. Lou, *Nanoscale*, 2012, **4**, 2526–2542.
- 15 X. J. Zhu, Y. W. Zhu, S. Murali, M. D. Stollers and R. S. Ruoff, *ACS Nano*, 2011, **5**, 3333–3338.
- 16 L. Pan, X. D. Zhu, X. M. Xie and Y. T. Liu, *Adv. Funct. Mater.*, 2015, **25**, 3341–3350.
- 17 W. Wei, S. B. Yang, H. X. Zhou, I. Lieberwirth, X. L. Feng and K. Mullen, *Adv. Mater.*, 2013, **25**, 2909–2914.
- 18 H. L. Fei, Z. W. Peng, L. Li, Y. Yang, W. Lu, E. L. G. Samuel, X. J. Fan and J. M. Tour, *Nano Res.*, 2014, **7**, 502–510.
- 19 Y. R. Wang, L. Zhang, X. H. Gao, L. Y. Mao, Y. Hu and X. W. Lou, *Small*, 2014, **10**, 2815–2819.
- 20 L. W. Su, Y. R. Zhong and Z. Zhou, *J. Mater. Chem. A*, 2013, **1**, 15158–15166.
- 21 C. N. He, S. Wu, N. Q. Zhao, C. S. Shi, E. Z. Liu and J. J. Li, *ACS Nano*, 2013, **7**, 4459–4469.
- 22 T. Yoon, C. Chae, Y. K. Sun, X. Zhao, H. H. Kung and J. K. Lee, *J. Mater. Chem.*, 2011, **21**, 17325–17330.
- 23 L. Wang, Y. Yu, P. C. Chen, D. W. Zhang and C. H. Chen, *J. Power Sources*, 2008, **183**, 717–723.
- 24 S. Zhu, M. Chen, J. Sun, J. Liu, T. Wu, H. Su, S. Qu, Y. Xie, S. Wang, X. Su and G. Diao, *RSC Adv.*, 2016, **6**, 58529–58540.
- 25 G. M. Zhou, D. W. Wang, P. X. Hou, W. S. Li, N. Li, C. Liu, F. Li and H. M. Cheng, *J. Mater. Chem.*, 2012, **22**, 17942–17946.
- 26 Y. He, L. Huang, J. S. Cai, X. M. Zheng and S. G. Sun, *Electrochim. Acta*, 2010, **55**, 1140–1144.
- 27 Y. Shi, J. Zhang, A. M. Bruck, Y. M. Zhang, J. Li, E. A. Stach, K. J. Takeuchi, A. C. Marschilok, E. S. Takeuchi and G. H. Yu, *Adv. Mater.*, 2017, **29**, 8.
- 28 J. M. Jeong, B. G. Choi, S. C. Lee, K. G. Lee, S. J. Chang, Y. K. Han, Y. B. Lee, H. U. Lee, S. Kwon, G. Lee, C. S. Lee and Y. S. Huh, *Adv. Mater.*, 2013, **25**, 6250–6255.
- 29 X. W. Li, L. Qiao, D. Li, X. H. Wang, W. H. Xie and D. Y. He, *J. Mater. Chem. A*, 2013, **1**, 6400–6406.
- 30 X. Xu, R. Cao, S. Jeong and J. Cho, *Nano Lett.*, 2012, **12**, 4988–4991.
- 31 M. V. Reddy, T. Yu, C. H. Sow, Z. X. Shen, C. T. Lim, G. V. S. Rao and B. V. R. Chowdari, *Adv. Funct. Mater.*, 2007, **17**, 2792–2799.
- 32 Y. Xu, Q. Liu, Y. Zhu, Y. Liu, A. Langrock, M. R. Zachariah and C. Wang, *Nano Lett.*, 2013, **13**, 470–474.
- 33 J. Z. Wang, C. Zhong, D. Wexler, N. H. Idris, Z. X. Wang, L. Q. Chen and H. K. Liu, *Chem.-Eur. J.*, 2011, **17**, 661–667.
- 34 L. W. Ji, Z. K. Tan, T. R. Kuykendall, S. Aloni, S. D. Xun, E. Lin, V. Battaglia and Y. G. Zhang, *Phys. Chem. Chem. Phys.*, 2011, **13**, 7170–7177.
- 35 O. Gerber, S. Begin-Colin, B. P. Pichon, E. Barraud, S. Lemonnier, C. Pham-Huu, B. Daffos, P. Simon, J. Come and D. Begin, *J. Energy Chem.*, 2016, **25**, 272–277.
- 36 F. Han, W. C. Li, D. Li and A. H. Lu, *J. Energy Chem.*, 2013, **22**, 329–335.
- 37 S. P. Zhu, M. Chen, W. J. Ren, J. R. Yang, S. S. Qu, Z. C. Li and G. W. Diao, *New J. Chem.*, 2015, **39**, 7923–7931.



38 A. Babaei, M. Zendehdel, B. Khalilzadeh and A. Taheri, *Colloids Surf. B*, 2008, **66**, 226–232.

39 J. Lu, X. L. Jiao, D. R. Chen and W. Li, *J. Phys. Chem. C*, 2009, **113**, 4012–4017.

40 Z. Li, Y. J. Chen, Y. K. Du, X. M. Wang, P. Yang and J. W. Zheng, *Int. J. Hydrogen Energy*, 2012, **37**, 4880–4888.

41 K. N. Kudin, B. Ozbas, H. C. Schniepp, R. K. Prud'homme, I. A. Aksay and R. Car, *Nano Lett.*, 2008, **8**, 36–41.

42 J. A. Zheng, C. A. Di, Y. Q. Liu, H. T. Liu, Y. L. Guo, C. Y. Du, T. Wu, G. Yu and D. B. Zhu, *Chem. Commun.*, 2010, **46**, 5728–5730.

43 J. Su, M. H. Cao, L. Ren and C. W. Hu, *J. Phys. Chem. C*, 2011, **115**, 14469–14477.

44 L. Fan, W. Zhang, S. Zhu and Y. Lu, *Ind. Eng. Chem. Res.*, 2017, **56**, 2046–2053.

45 S. Laruelle, S. Gruegeon, P. Poizot, M. Dolle, L. Dupont and J. M. Tarascon, *J. Electrochem. Soc.*, 2002, **149**, A627–A634.

46 Y. Chen, B. H. Song, X. S. Tang, L. Lu and J. M. Xue, *Small*, 2014, **10**, 1536–1543.

47 Y. Suo, Q. Q. Zhao, J. K. Meng, J. Li, X. C. Zheng, X. X. Guan, Y. S. Liu and J. M. Zhang, *Mater. Lett.*, 2016, **174**, 36–39.

